

Quantitative Histopathological Validation of Bioprinted Tissue Models in Early Stage Oral Submucous Fibrosis

Vinit and Kanika Singroha

Cellverse Pvt. Ltd., India

`vineet10338@gmail.com`, `kanika.singroha@cellverse.org`,

Abstract. Oral Submucous Fibrosis (OSMF) is a progressive fibrotic disorder of the oral mucosa with high malignant potential. Existing models have contributed to OSMF research but cannot capture the complex tissue organization needed to study disease progression and test interventions effectively. While 3D bioprinting offers a promising route for developing in-vitro disease models, validating the pathological fidelity of these constructs remains challenging due to reliance on subjective histological evaluation. We propose a deep learning-based framework for objective, quantitative validation of bioprinted OSMF tissue, centered on two key histopathological markers: (i) the ratio of fine to bundled collagen fibres and (ii) zone-wise cellular density. Our framework first establishes grade-specific marker distributions from real OSMF cases spanning all four clinical grades using histopathological images analyzed with attention-enhanced deep learning models. These models—ParNet-integrated ResNeXt50 for fibre classification and U-Net++ for nuclei segmentation—achieved 97.87% accuracy and a Dice loss of 0.226, respectively, despite limited training data. We then applied the same analysis pipeline to 3D bioprinted tissue constructs engineered to mimic OSMF features. The bioprinted samples exhibited fibre composition and cellularity profiles closely matching early-stage OSMF, confirming their pathological fidelity and demonstrating the framework’s potential for rigorous validation of bioprinted disease models.

Keywords: Oral Submucous Fibrosis · Bioprinting Validation · Quantitative Tissue Analysis

1 Introduction

Oral Submucous Fibrosis (OSMF) is a chronic, potentially malignant disorder of the oral mucosa, primarily linked to areca nut consumption and prevalent across South and Southeast Asia [1]. Characterized by progressive collagen deposition, epithelial atrophy, and restricted mouth opening, OSMF remains difficult to treat due to limited understanding of its progression and the absence of robust preclinical models [2].

Traditional approaches—including 2D cell cultures and animal models using bleomycin-induced fibrosis in Wistar rats [3]—offer partial insights but fall short

in replicating the complex, graded pathology observed in humans. Recent advances in 3D bioprinting have enabled the fabrication of oral tissue constructs and fibrotic disease models, including those for liver and lung fibrosis [4, 5]. However, validating the pathological fidelity of bioprinted constructs remains a major challenge, often relying on subjective histological interpretation with limited reproducibility and scalability.

In parallel, deep learning has revolutionized histopathology by automating key tasks including classification [6], gland and nuclei detection [7], morphological characterization [8], and biomarker quantification [9]. CNNs and transformer-based models now match or exceed pathologists in grading tumors, predicting genetic mutations, and extracting spatial patterns from H&E-stained slides. These advances enable objective and reproducible analysis of complex histological structures, supporting applications from disease diagnosis to prognosis. Although widely applied to patient-derived clinical tissue, its use for validating engineered disease models, such as bioprinted constructs, remains underexplored.

This work addresses that gap by introducing an AI-driven validation framework tailored to OSMF. We quantify two key histopathological hallmarks: (i) the ratio of fine to bundled collagen fibers and (ii) zone-wise cellular density to establish disease-specific metrics from real, clinically graded OSMF biopsy images. These metrics are then applied to 3D bioprinted constructs engineered to replicate early-stage OSMF. Through this comparison, we offer a reproducible and quantitative method to assess the fidelity of bioprinted disease models against the pathology of the real patient.

2 Dataset Specification

Four datasets were used to support different components of the proposed framework: NuInsSeg for nuclei segmentation model training, a custom Fibres dataset for fibrosis classification model training, the primary OSMF dataset for study and analysis of disease specific markers, and the bioprinted tissue image dataset for validation with real OSMF tissue.

2.1 NuInsSeg Dataset

The NuInsSeg dataset [10] comprises 665 H&E-stained image patches with over 30,000 annotated nuclei from diverse human and mouse tissues. It was used to train the segmentation model for nuclei segmentation, enabling accurate cellular density estimation in OSMF images.

2.2 OSMF Dataset

The primary dataset consists of 41 H&E-stained histological images of clinically graded OSMF tissue (Grades 1–4), captured at $20\times$ magnification and annotated by an expert pathologist. These served as the ground truth for validating fibrosis quantification and cell density estimation.

Table 1: Distribution of OSMF histopathology images by fibrosis grade.

Grade 1	Grade 2	Grade 3	Grade 4	Total
3	15	18	5	41

2.3 Bioprinted Tissue Dataset

This dataset comprises 15 H&E-stained histopathology images of the bioprinted tissue construct, captured at $20\times$ magnification using the same microscope as for OSMF images. These images were analyzed with the trained models to quantitatively validate the fidelity of the bioprinted tissue against real OSMF histology.

2.4 Fibres Dataset

A curated dataset of 310 image patches was created for fibrosis classification, with 166 labeled as fine fibres and 144 as bundled fibres. The images were sourced from OSMF and other oral mucosal tissues. This dataset was used to train the classification model, with augmentation applied to improve robustness.

Table 2: Composition of the curated Fibres dataset.

Fibre Category	Number of Images
Fine fibres	166
Bundled fibres	144
Total	310

3 Methodology

The proposed framework utilizes deep learning models to quantitatively validate 3D bioprinted tissue constructs of early-stage OSMF by analyzing two key histopathological features: fibrosis type and cell density (Fig. 2).

3.1 Bioprinted Tissue Preparation

Bioprinted constructs were made with a bioink of gum tragacanth, carboxymethyl chitosan, gelatin, and sodium alginate, seeded with human gingival fibroblasts and umbilical vein endothelial cells to replicate oral mucosal structure. Fibrotic changes were induced using 'Paan' extract over a set period to mimic early-stage OSMF.

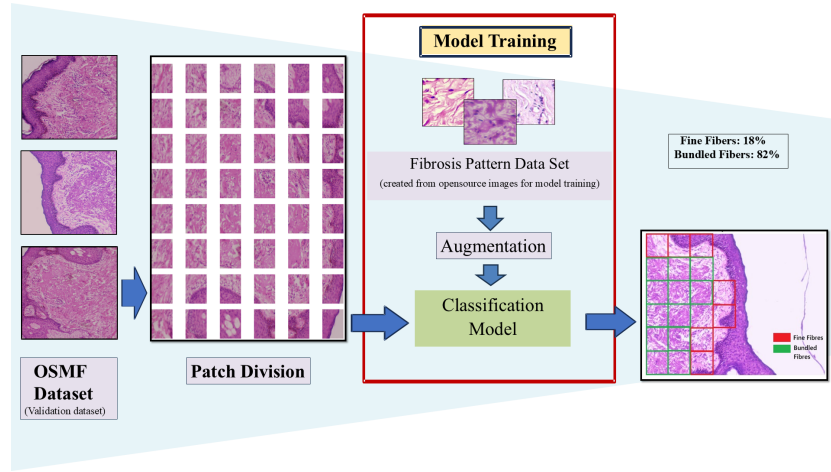


Fig. 1: Pipeline for fibrosis pattern quantification.

3.2 Fibrosis Type Quantification

Fibrosis regions were initially identified using a simple CNN-based region detector. The fibrosis detector is a simple CNN (two conv layers, ReLU, 2-layer MLP) trained on about 250 patches (fibrosis, non-fibrosis regions), achieving 94.2% accuracy. Its role was to isolate connective tissue regions before analysis. Subsequently, a deep learning classifier was developed to categorize fibrosis patches into fine or bundled fibre phenotypes. The model integrates lightweight, untrained ParNet [11] modules between frozen Imagenet pre-trained ResNeXt50 [12] blocks to enhance feature extraction while mitigating overfitting risks due to limited data. Each ParNet module employs parallel 1×1 convolution, 3×3 convolution, and Skip-Squeeze-and-Excitation [13] branches. The trained model outputs the proportion of fine and bundled fibres across all OSMF and bioprinted tissue samples. Figure 1 shows an overview of the process.

3.3 Cell Density Evaluation

For cellular analysis, an enhanced U-Net++ [14] architecture was employed, incorporating ParNet attention modules within its ResNet encoder. The model was trained and validated on the NuInSeg dataset to achieve robust nuclei segmentation across diverse histological contexts. Nuclei counts were computed within predefined regions to derive cell density. Zone-wise connected component analysis was performed, with Zone 1 defined as the superficial region (200 pixels beneath the epithelial surface) and Zone 2 representing deeper connective tissue. This spatial quantification enabled comparative analysis of cellularity patterns between OSMF grades and bioprinted tissues.

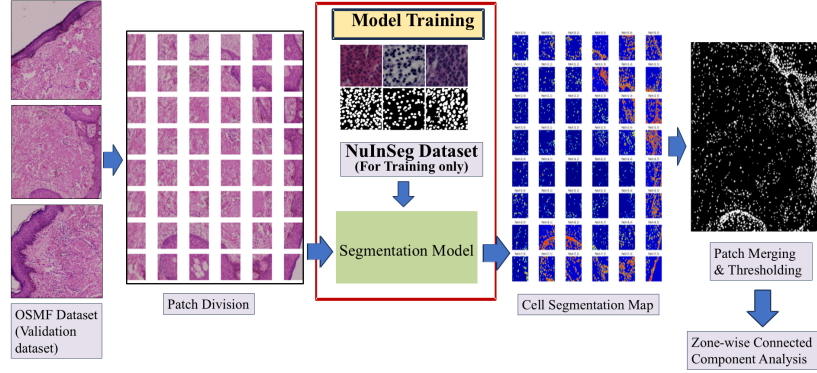


Fig. 2: Pipeline for cell density estimation.

4 Results and Analysis

This section presents the experimental setup, followed by the results of fibrosis classification and cell density estimation, demonstrating the framework’s ability to capture clinically relevant features of OSMF progression.

Table 3: Classification Parameters

Parameter	Value
Loss Function	Cross-Entropy
Optimizer	Adam (LR = 1×10^{-4})
Scheduler	Cosine Annealing
Weight Decay	0.1
Batch Size	24
Epochs	15
Patch Size	128×128

Table 4: Segmentation Parameters

Parameter	Value
Loss Function	Dice + Jaccard
Optimizer	Adam (LR = 1×10^{-4})
Scheduler	ReduceLROnPlateau
Weight Decay	1×10^{-6}
Batch Size	16
Epochs	50
Patch Size	256×256

4.1 Experimental Setup

The fibrosis model was trained on 310 image patches (166 fine, 144 bundled fibres), split 80:20 for training and validation. Augmentations (elastic transformations, color jitter, contrast adjustments, CLAHE, spatial flips) expanded the training set to 744 patches for better generalization. Table 3 and Table 4 show the experimental setup used to train the two models.

For nuclei segmentation, U-Net++ was trained on NuInsSeg and applied to OSMF images for density calculation. Inputs were normalized and resized to

256×256 pixels. Classification was assessed with accuracy, precision, recall, and F1-score; segmentation used Dice and Jaccard loss metrics.

Table 5: Performance of baseline architectures for fibrosis classification.

Base Model	Category	Accuracy	Precision	Recall	F1-score
ResNet50 [15]	CNN	85.80	86.0	85.5	85.75
ResNeXt50 [12]	CNN++	87.05	87.5	86.8	87.15
EfficientNet B0 [16]	CNN	79.11	79.5	78.9	79.2
SL-ViT [17]	Transformer	80.81	81.2	80.3	80.75
MobileViT-xs [18]	Conv+Transformer	86.10	86.4	85.8	86.1

Table 6: Effect of attention modules on fibrosis classification performance.

Attention Mechanism	Accuracy	Precision	Recall	F1-score
CBAM [19]	0.9197	0.9202	0.9197	0.9197
ECA Attention [20]	0.9149	0.9194	0.9118	0.9139
Halo Attention [21]	0.9574	0.9573	0.9573	0.9573
Triplet Attention [22]	0.9149	0.9145	0.9145	0.9145
ParNet Attention [11]	0.9787	0.9808	0.9773	0.9786

4.2 Fibrosis Type Classification Results

The fibrosis classifier was initially evaluated across several baseline architectures (Table 5). ResNeXt50 achieved the highest baseline accuracy of 87.05%. Incorporating attention modules further improved performance, with the ParNet attention integrated ResNeXt50 achieving 97.87% accuracy and an F1-score of 97.86% (Table 6).

Applying the model to full OSMF tissue images revealed a consistent trend of increasing bundled fibre proportion with fibrosis grade progression (Fig. 3). Quantitative analysis across 41 OSMF images confirmed this pattern, capturing a histopathologically meaningful shift in collagen architecture from early to advanced grades.

Statistical analysis shows that the Fibre composition differences were strongly significant ($H = 17.26$, $p = 0.00063$; $\epsilon^2 = 0.385$, large effect size) with post-hoc analysis confirming Grade 2 vs Grade 3: $p = 0.0037$ as a major point of separation. Correlation analysis further supported biological consistency (e.g., fine fibrils $\rho = -0.63$, $p = 0.00001$; bundled fibres $\rho = +0.63$, $p = 0.00001$).

4.3 Cell Density Estimation Results

For nuclei segmentation, U-Net++ achieved the best baseline performance (Dice loss 0.264, Jaccard loss 0.418), outperforming other models including Segformer

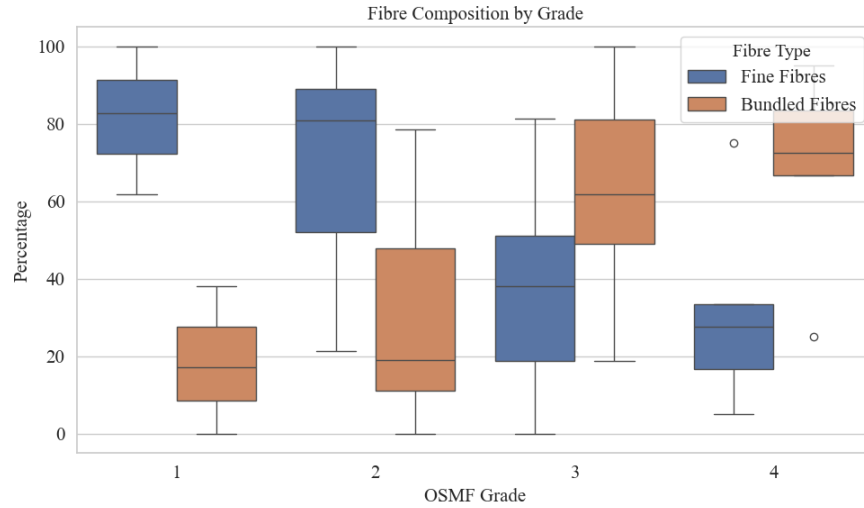


Fig. 3: Fibre composition across OSMF grades. AI-based quantification shows a progressive decline in fine fibres and corresponding rise in bundled fibres with increasing disease severity.

Table 7: Segmentation performance of baseline models on nuclei detection.

Model	Dice Loss	Jaccard Loss
U-Net [23]	0.266	0.420
SegFormer [24]	0.317	0.481
DeepLabv3 [25]	0.362	0.531
U-Net++ [14]	0.264	0.418

and DeepLab (Table 7). Incorporating Parnet attention further improved segmentation (Dice loss 0.226, Jaccard loss 0.368) as shown in Table 8.

The analysis showed significant grade-wise differences (Kruskal–Wallis $H = 13.64$, $p = 0.0034$) with post-hoc tests confirming pairwise significance (e.g., Grade 2 vs Grade 3: $p = 0.026$; Grade 3 vs Grade 4: $p = 0.009$). Zone-wise cellular density was computed across all OSMF grades, revealing a strong positive correlation ($r = 0.692$) between superficial (Zone 1) and deep (Zone 2) regions. Moreover, a consistent decline in cell density was observed with increasing fibrosis grade (Fig. 4), consistent with reduced fibroblast activity in advanced fibrosis.

4.4 Bioprinted Tissue Validation

Table 9 compares bioprinted tissue with each OSMF grade. The bioprinted construct displayed 98.2% fine fibres and no bundled fibres, closely matching early-stage (Grade 1/2) OSMF. Its cell density (0.000339 cells/px²) showed minimal

Table 8: Effect of attention modules on nuclei segmentation performance.

Attention Mechanism	Dice Loss	Jaccard Loss
CBAM	0.241	0.387
ECA Attention	0.239	0.384
Halo Attention	0.236	0.382
Triple Attention	0.231	0.376
ParNet Attention	0.226	0.368

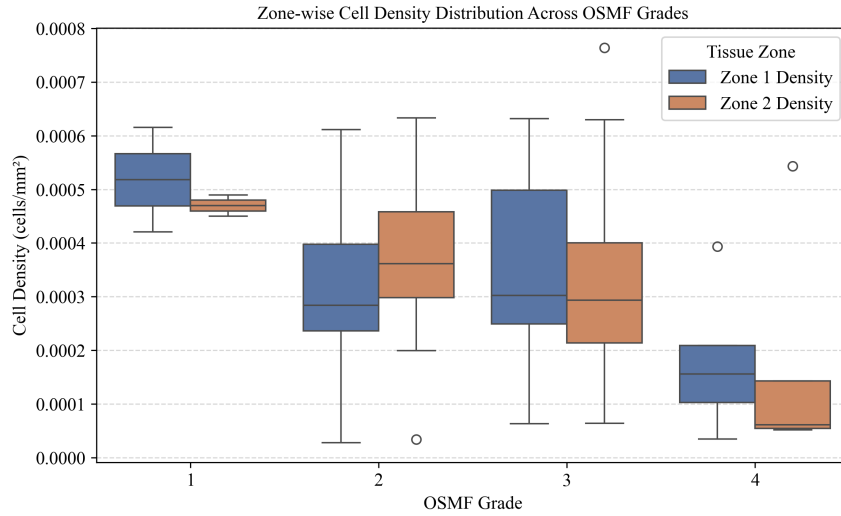


Fig. 4: Zone-wise cell density across OSMF grades. Cellularity declines consistently from Grade 1 to Grade 4, especially in deeper tissue zones, highlighting fibroblast reduction with disease progression.

deviation from Grade 2 (1.46%) and significant divergence from Grades 3–4. These results confirm the construct mimics early-stage fibrosis, validating both the tissue model and the AI-based framework.

5 Discussion and Conclusion

This study presents a compact, interpretable framework for validating bioprinted OSMF models using AI-derived histopathological metrics. By quantifying fibrosis morphology and cellularity—two complementary disease markers—the method enables objective alignment of engineered tissue with real pathological grades.

The bioprinted construct exhibited histological profiles comparable to early-stage OSMF (Grade 1–2), validating both the model’s fidelity and the analytical robustness of the pipeline. This resolves a key gap in 3D bioprinting: the absence of reproducible validation metrics beyond subjective histological review.

Table 9: Histopathological Validation of Bioprinted Tissue Against Real OSMF Tissue.

Sample	Fine Fibres (%)	Bundled Fibres (%)	Cell Density (cells/px ²)	% Diff. (Fibres)	% Diff. (Density)
Grade 1 OSMF	83.55 ± 19.08	16.45 ± 19.08	0.000270 ± 0.000375	17.53%	22.45%
Grade 2 OSMF	71.46 ± 25.15	28.54 ± 25.15	0.000334 ± 0.000133	37.41%	1.46%
Grade 3 OSMF	34.93 ± 24.17	65.07 ± 24.17	0.000513 ± 0.000159	181.11%	-33.80%
Grade 4 OSMF	31.52 ± 26.61	68.48 ± 26.61	0.000176 ± 0.000170	211.58%	93.11%
Bioprinted Tissue	97.20 ± 2.50	2.80 ± 2.50	0.000339 ± 0.000015	-	-

Notes: Fibre percentages and cell density are AI-derived from H&E images.
Differences are relative to bioprinted values. 1 px² = 0.0961 μm^2 .

More broadly, this framework introduces a generalizable paradigm for AI-assisted evaluation of engineered disease models. This study is limited by the small dataset size and lack of pathologist comparison, which may affect generalizability. Future work will expand validation across multi-center cohorts and integrate multimodal data to enhance clinical relevance.

References

1. J. Tang *et al.*, “Oral submucous fibrosis: pathogenesis and therapeutic approaches,” *International Journal of Oral Science*, vol. 17, p. 8, Feb. 2025.
2. L. Zhang, J. Chen, F. Li, B. Liu, and J. Liu, “Choosing the proper animal model for oral submucous fibrosis research: considerations and challenges,” *Frontiers in Physiology*, vol. 16, p. 1501158, 2025.
3. M. U. Piracha, I. Ejaz, S. Chaudhry, and S. Ghafoor, “Formulation of in-vivo experimental model of oral submucous fibrosis in wistar rat,” *Pakistan Journal of Medical and Health Sciences*, vol. 16, pp. 241–244, Nov. 2022.
4. T. Almela, L. Tayebi, and K. Moharamzadeh, “3d bioprinting for in vitro models of oral cancer: Toward development and validation,” *Bioprinting*, vol. 22, p. e00132, June 2021.
5. F. Zhao, Z. Zhang, and W. Guo, “The 3-dimensional printing for dental tissue regeneration: the state of the art and future challenges,” *Frontiers in Bioengineering and Biotechnology*, vol. 12, p. 1356580, Feb. 2024.
6. J. Noorbakhsh, S. Farahmand, A. Foroughi Pour, S. Namburi, D. Caruana, D. Rimm, ..., and J. H. Chuang, “Deep learning-based cross-classifications reveal conserved spatial behaviors within tumor histological images,” *Nature Communications*, vol. 11, no. 1, p. 6367, 2020.
7. J. M. Bokhorst, I. D. Nagtegaal, F. Fraggetta, S. Vatrano, W. Mesker, M. Vieth, ..., and F. Ciompi, “Deep learning for multi-class semantic segmentation enables colorectal cancer detection and classification in digital pathology images,” *Scientific Reports*, vol. 13, no. 1, p. 8398, 2023.
8. Y. Ge, J. Leng, Z. Tang, K. Wang, K. U, S.-M. Zhang, ..., and J. Zhao, “Deep learning-enabled integration of histology and transcriptomics for tissue spatial profile analysis,” *Research*, vol. 8, p. 0568, 2025.

9. M. Pizurica, Y. Zheng, F. Carrillo-Perez, H. Noor, W. Yao, C. Wohlfart, ..., and O. Gevaert, "Digital profiling of gene expression from histology images with linearized attention," *Nature Communications*, vol. 15, no. 1, p. 9886, 2024.
10. A. Mahbod, C. Polak, K. Feldmann, R. Khan, K. Gelles, G. Dorffner, R. Woitek, S. Hatamikia, and I. Ellinger, "Nuinsseg: A fully annotated dataset for nuclei instance segmentation in h&e-stained histological images," *arXiv.org*, vol. abs/2308.01760, aug 2023.
11. A. Goyal, A. Bochkovskiy, J. Deng, and V. Koltun, "Non-deep Networks," *Advances in Neural Information Processing Systems*, vol. 35, pp. 6789–6801, 2022.
12. S. Xie, R. Girshick, P. Dollár, Z. Tu, and K. He, "Aggregated residual transformations for deep neural networks," in *Proceedings of the IEEE conference on computer vision and pattern recognition*, pp. 1492–1500, 2017.
13. J. Hu, L. Shen, and G. Sun, "Squeeze-and-excitation networks," in *Proceedings of the IEEE conference on computer vision and pattern recognition*, pp. 7132–7141, 2018.
14. Z. Zhou, M. M. Rahman Siddiquee, N. Tajbakhsh, and J. Liang, "Unet++: A nested u-net architecture for medical image segmentation," in *Deep learning in medical image analysis and multimodal learning for clinical decision support: 4th international workshop, DLMIA 2018, and 8th international workshop, ML-CDS 2018, held in conjunction with MICCAI 2018, Granada, Spain, September 20, 2018, proceedings 4*, pp. 3–11, Springer, 2018.
15. K. He, X. Zhang, S. Ren, and J. Sun, "Deep residual learning for image recognition," in *Proceedings of the IEEE conference on computer vision and pattern recognition*, pp. 770–778, 2016.
16. M. Tan and Q. V. Le, "Efficientnet: Rethinking model scaling for convolutional neural networks," in *International conference on machine learning*, pp. 6105–6114, PMLR, 2019.
17. Z. Liu, Y. Lin, Y. Cao, H. Hu, Y. Wei, Z. Zhang, S. Lin, and B. Guo, "Swin transformer: Hierarchical vision transformer using shifted windows," in *Proceedings of the IEEE/CVF International Conference on Computer Vision*, pp. 10012–10022, 2021.
18. S. Mehta and M. Rastegari, "Mobilevit: Light-weight, general-purpose, and mobile-friendly vision transformer," *arXiv preprint arXiv:2110.02178*, 2021.
19. S. Woo, J. Park, J.-Y. Lee, and I. S. Kweon, "CBAM: Convolutional Block Attention Module," in *Proceedings of the European Conference on Computer Vision (ECCV)*, pp. 3–19, 2018.
20. Q. Wang, B. Wu, P. Zhu, P. Li, W. Zuo, and Q. Hu, "ECA-Net: Efficient Channel Attention for Deep Convolutional Neural Networks," in *Proceedings of the IEEE/CVF Conference on Computer Vision and Pattern Recognition (CVPR)*, pp. 11534–11542, 2020.
21. A. Vaswani, P. Ramachandran, A. Srinivas, N. Parmar, B. Hechtman, and J. Shlens, "Scaling Local Self-Attention for Parameter Efficient Visual Backbones," in *Proceedings of the IEEE/CVF Conference on Computer Vision and Pattern Recognition (CVPR)*, pp. 12894–12904, 2021.
22. D. Misra, T. Nalamada, A. U. Arasanipalai, and Q. Hou, "Rotate to Attend: Convolutional Triplet Attention Module," in *Proceedings of the IEEE/CVF Winter Conference on Applications of Computer Vision (WACV)*, pp. 3139–3148, 2021.
23. O. Ronneberger, P. Fischer, and T. Brox, "U-net: Convolutional networks for biomedical image segmentation," in *International Conference on Medical image computing and computer-assisted intervention*, pp. 234–241, Springer, 2015.

24. E. Xie, W. Wang, Z. Yu, A. Anandkumar, J. M. Alvarez, and P. Luo, “Segformer: Simple and efficient design for semantic segmentation with transformers,” in *Advances in Neural Information Processing Systems*, vol. 34, pp. 12077–12090, 2021.
25. L.-C. Chen, G. Papandreou, F. Schroff, and H. Adam, “Rethinking atrous convolution for semantic image segmentation,” *arXiv preprint arXiv:1706.05587*, 2017.